



Three-dimensional Global Hybrid Simulations of Flux Transfer Event Showers at Mercury

Quanming Lu^{1,2} , Jin Guo^{1,2} , San Lu^{1,2} , Xueyi Wang³, James A. Slavin⁴ , Weijie Sun⁴ , Rongsheng Wang^{1,2} , Yu Lin³, and Jun Zhong⁵

¹ CAS Key Lab of Geospace Environment, School of Earth and Space Sciences, University of Science and Technology of China, Hefei, People's Republic of China
qmlu@ustc.edu.cn; lusan@ustc.edu.cn

² CAS Center for Excellence in Comparative Planetology, Hefei, People's Republic of China

³ Department of Physics, Auburn University, Auburn, AL, USA

⁴ Department of Climate and Space Sciences and Engineering, University of Michigan, Ann Arbor, MI, USA

⁵ Key Laboratory of Earth and Planetary Physics, Institute of Geology and Geophysics, Chinese Academy of Sciences, Beijing, People's Republic of China

Received 2022 June 22; revised 2022 August 17; accepted 2022 August 21; published 2022 September 15

Abstract

One of the important MESSENGER observations is the formation of flux transfer event (FTE) showers, where tens of FTEs are observed in a short time interval of about 1–2 minutes, at Mercury's magnetopause. In this paper, we investigate the interactions between the solar wind and Mercury's magnetosphere using three-dimensional global hybrid simulations. When the interplanetary magnetic field (IMF) is purely southward, we can observe FTE showers at the low-latitude dayside magnetopause, and these FTEs can propagate northward or southward with a speed of about 90 km s^{-1} . When the IMF is purely northward, FTE showers can be produced in both the northward and southward hemispheres of the high-latitude nightside magnetopause, and these FTEs propagate toward the magnetotail with a speed of about 250 km s^{-1} . The typical FTEs have a duration of 1–2 s, and reoccur in 5–6 s. Our simulations provide a good explanation for FTE showers observed by MESSENGER.

Unified Astronomy Thesaurus concepts: Planetary magnetospheres (997); Mercury (planet) (1024); Solar magnetic reconnection (1504); Planetary boundary layers (1245); Solar-planetary interactions (1472)

1. Introduction

Flux transfer events (FTEs), a series of distinct bipolar perturbations in the magnetic field component normal to the planetary magnetopause, topologically connect the interplanetary and planetary magnetic fields in the magnetopause (Russell & Elphic 1978), and provide a channel for mass and energy from the solar wind to the planetary magnetosphere (Lockwood & Moen 1999; Paschmann et al. 1982; Hasegawa et al. 2006; Kuznetsova et al. 2009; Tan et al. 2011; Dong et al. 2017; Sun et al. 2022). It is generally believed that FTEs are essentially magnetic flux ropes formed in multiple X-line reconnection occurring in the magnetopause current sheet (Lee & Fu 1985; Zhong et al. 2013; Fuselier et al. 2018; Guo et al. 2020). FTEs were first reported at the magnetopause of Earth with the ISEE satellite (Russell & Elphic 1978), and now are commonly observed in other magnetized planetary magnetopauses (Russell & Walker 1985; Jasinski et al. 2016).

Mercury has its own intrinsic magnetic field with a dipolar magnetic moment closely aligned with the rotation axis and a northward offset of about $0.2R_M$ (R_M is Mercury's radius, which is about 2440 km) (Anderson et al. 2008, 2011). The interaction of Mercury's relative weak magnetic field with the solar wind produces a miniature magnetosphere with a subsolar distance of about $1.5R_M$ (e.g., Slavin et al. 2008). FTEs at Mercury's magnetopause were first discovered by Russell & Walker (1985) with the Mariner 10 spacecraft. The measurements from Mercury Surface, Space Environment, Geochemistry, and Ranging (MESSENGER, launched in 2004), provide

not only more details of Mercury's global dipolar magnetic field, but also the characteristics of FTEs at the magnetopause. Slavin et al. (2012) found that the rate of reconnection occurring in the magnetopause current sheet of Mercury is much faster than that at Earth, which may be caused by the stronger interplanetary magnetic field (IMF) in Mercury's orbit. The consequent FTEs are usually produced in the form of a large number (>10) during a short time interval (one to several minutes), which is named as an "FTE shower." During a typical FTE shower, each FTE has the duration of about 1–2 s, and the separation between two neighboring FTE centers is about 5–6 s (Sun et al. 2020). An FTE shower can occur at the low-latitude dayside magnetopause when the IMF has a southward component, as well as at the high-latitude nightside magnetopause when the IMF has a northward component (Sun et al. 2020; Zhong et al. 2020; Sun et al. 2022). Therefore, the properties of FTEs in Mercury's magnetopause are much different from those at Earth, where the duration of FTE ranges from about 1–2 minutes and the separation is about 8 minutes (Rijnbeek et al. 1984). However, due to the limited availability of particle data, it is difficult to reveal the underlying mechanism for FTE showers at Mercury's magnetopause with satellite observations.

In this paper, we investigate the interaction between the solar wind and Mercury's magnetic field with a global three-dimensional (3D) hybrid simulation code; we show that magnetic reconnection can occur at the magnetopause, and FTEs are produced in a quasiperiodic manner. When the IMF points southward, FTEs are formed at the low-latitude dayside magnetopause, while FTEs appear at the high-latitude nightside magnetopause when the IMF points northward. The results provide a good explanation for FTE shower observed by MESSENGER.

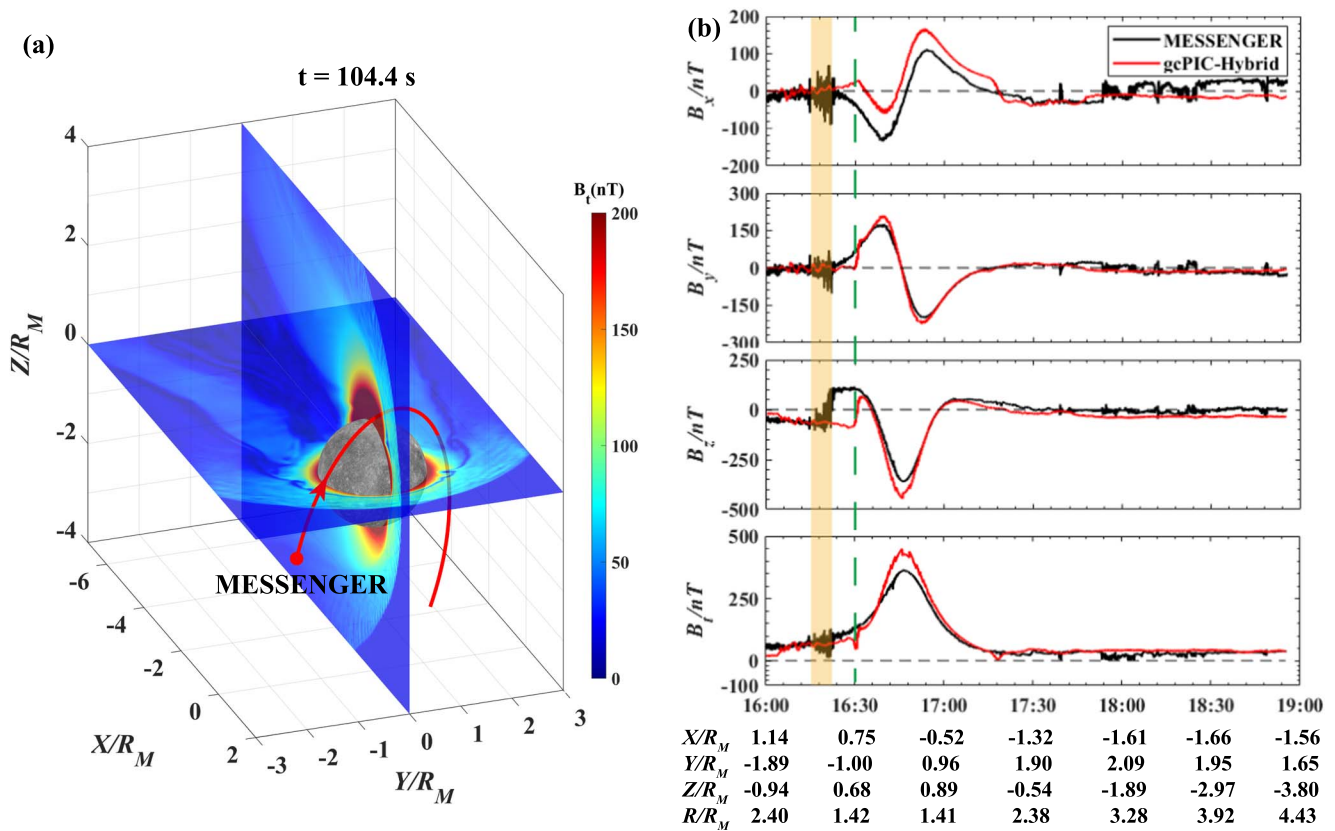


Figure 1. The comparison of magnetic field obtained from our gcPIC-hybrid simulation in Case 1 with that in time following the MESSENGER orbit related to the observation on 2013 June 18. (a) The amplitude of magnetic field in the noon–midnight meridian and equatorial planes obtained from the simulation at $t = 104.04$ s, and the MESSENGER’s trajectory on 2013 June 18 is plotted in red. (b) The magnetic field from the MESSENGER observation on 2013 June 18. The magnetic field from the simulation at $t = 104.04$ s, which is obtained along the satellite trajectory denoted by the red line in (b), is also exhibited for reference. The vertical shaded region with the yellow color and vertical green dashed line denote respectively the intervals in the observation and simulation, where FTEs are formed.

2. Simulation Model

In this paper, a 3D global hybrid code is employed to simulate the interactions between Mercury’s magnetic field and the solar wind. In hybrid simulations, ions are treated as particles, and electrons are assumed as a massless fluid. The code is named as gcPIC-hybrid, and gcPIC is a software package that can implement kinetic simulations (including full particle simulation and hybrid simulation) in a general curvilinear coordinate system. The software package has been successfully performed to study the excitation of chorus waves in a dipole magnetic field (Lu et al. 2019). The Mercury solar orbital coordinate system is adopted in the simulations with the domain size $-7R_M \leq x \leq 3R_M$, $-3R_M \leq y \leq 3R_M$, and $-4R_M \leq z \leq 4R_M$. There are $N_x \times N_y \times N_z = 493 \times 250 \times 377$ grids, and about 2.4×10^9 particles. A nonuniform system of grid cells is used, with the size about $\Delta x = \Delta z = 0.015R_M$ and $\Delta y = 0.02R_M$ near the magnetopause. The time step is chosen as $\Omega_{i0}\Delta t = 0.02$, where Ω_{i0} is the ion gyrofrequency based on the intensity of IMF.

Mercury is assumed to be a spherical object without an exosphere, and the particles are absorbed at the surface. The conducting boundary conditions for electromagnetic fields are applied at the core surface ($0.8R_M$). Mercury’s dipole moment is $190 \text{ nT} \cdot R_M^3$ along the z direction, with an $0.2R_M$ offset northward from the center of the planet (Anderson et al. 2011). Initially, the dipole magnetic field is confined to $x \leq 2R_M$ by adding an image dipole. A uniform solar wind carrying the steady IMF is filled in the region $x > 2R_M$ with the frontside boundary at $x = 3R_M$. The parameters for the solar wind are

described as follows: the flow velocity is $U_0 = (-400, 0, 0)$ km s^{-1} , the number density is $N_0 = 40 \text{ cm}^{-3}$, and the temperature is 15 eV. We run two cases. In Case 1, the IMF is purely southward, and the magnetic field is $\mathbf{B}_0 = (0, 0, -20)$ nT. A purely northward IMF is used in Case 2, with the magnetic field $\mathbf{B}_0 = (0, 0, 20)$ nT. Therefore, the ion inertial length $d_{i0} \approx 36.0$ km, the ion gyrofrequency $\Omega_{i0}^{-1} \approx 0.5$ s, the ion and electron plasma is $\beta_{i0} = \beta_{e0} \approx 0.6$, the Alfvén velocity is $V_{A0} \approx 68.9 \text{ km s}^{-1}$, and the Alfvén Mach number is $M_{A0} \approx 5.8$. The grid size near the magnetopause is smaller than or around the ion inertial length. The outflow boundary conditions are used at $x = -7R_M$, $y = \pm 3R_M$, and $z = \pm 4R_M$.

3. Simulation Results

The IMF in the solar wind is purely southward in Case 1. In Figure 1, we compare the magnetic field from our gcPIC-hybrid simulation in Case 1 with that in time following the MESSENGER orbit related to the observation on 2013 June 18, where the IMF is predominated by the southward component. Figure 1(a) shows the amplitude of the magnetic field in the noon–midnight meridian and equatorial planes obtained from the simulation at $t = 104.04$ s, and the MESSENGER’s trajectory on 2013 June 18 is plotted in red, pointing from the dayside/dawnside to the dayside/duskside. Figure 1(b) plots the magnetic field from the MESSENGER observation on 2013 June 18. In the figure, the magnetic field from the simulation at $t = 104.04$ s, which is obtained along the satellite trajectory denoted by the red line in Figure 1(b), is also

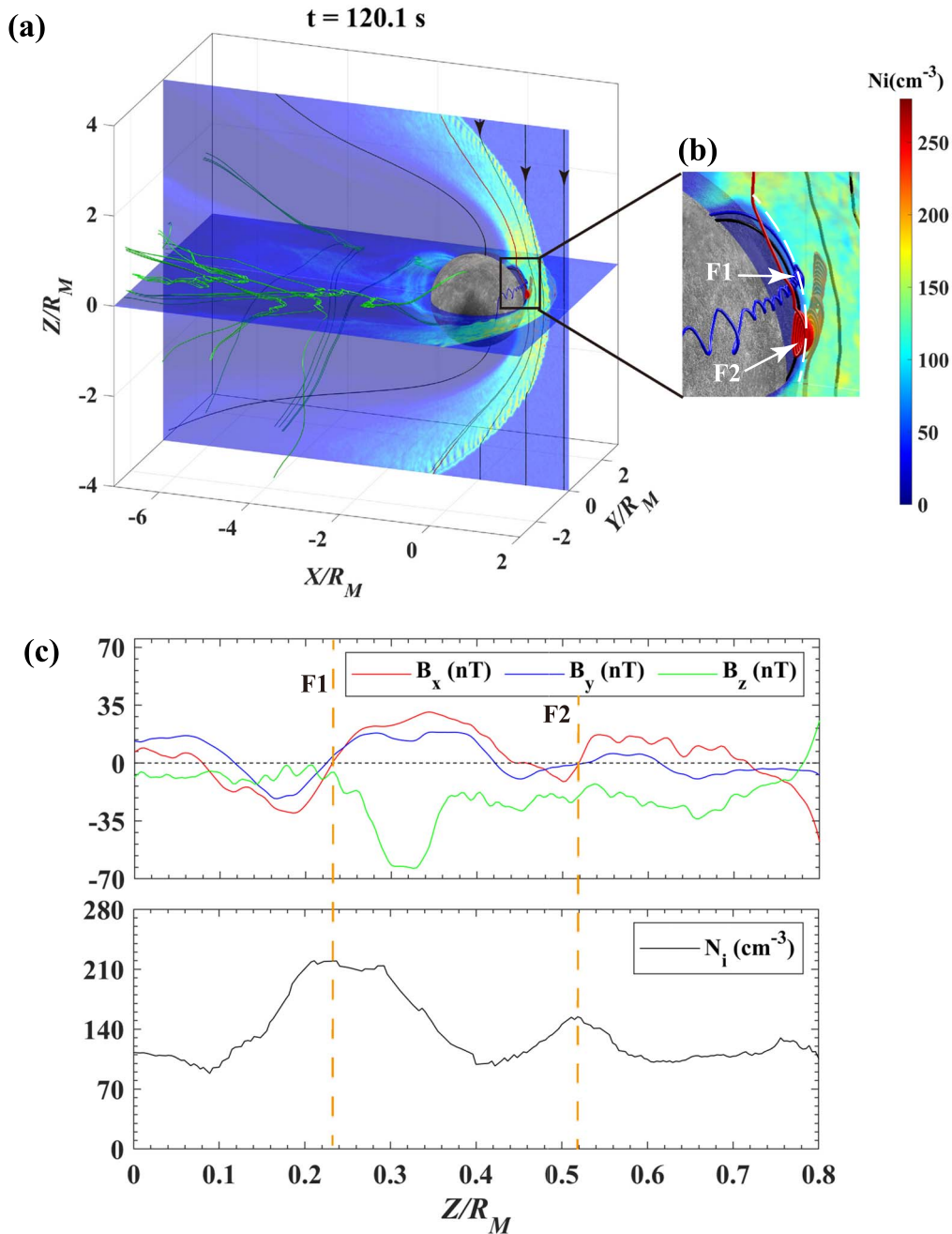


Figure 2. 3D view of Mercury’s magnetosphere obtained from our hybrid simulation at $t = 120.10$ s in Case 1. (a) The ion number density N_i in the noon–midnight meridian and equatorial planes. The magnetic structure of flux ropes is represented by 3D magnetic field lines with different colors (red, blue, and green). (b) The enlarged view of the denoted region in (a), and F1–2 represent two FTEs. (c) Three components of the magnetic field (B_x , B_y , and B_z) and the ion number density N_i along the dashed line in (b).

exhibited for reference. We can find that the magnetic field along the satellite trajectory in the simulation is consistent with that in the observation. The satellite is initially in the magnetosheath and crosses the magnetopause around 16:22 and 16:30 in the observation and simulation, respectively. FTEs can be observed around the magnetopause in both the satellite observation and simulation, and the observation event has been reported by Sun et al. (2020). The magnetic field is about $\mathbf{B} = (-18, -9, -54)$ nT in the observation and $\mathbf{B} = (-9, -2, -55)$ nT in the simulation just before the satellite cross the magnetopause. The amplitude of the magnetic field is greatly enhanced in the magnetosphere.

In Case 1, magnetic reconnection occurs between the southward magnetic field in the solar wind and Mercury’s magnetic field at the low-latitude dayside magnetopause. It is triggered at about $t = 10$ s, and at this time the subsolar distance of the magnetosphere is about $1.3 R_M$. The magnetic fluxes are then convected toward the magnetotail, leading to the triggering of magnetotail reconnection at about $t = 70$ s. Figure 2(a) plots the 3D view of Mercury’s magnetosphere obtained with hybrid simulation at $t = 120.01$ s in Case 1, showing the ion number density N_i in the noon–midnight meridian and equatorial planes, the magnetic field lines in the noon–midnight meridian plane, and the magnetic structures of

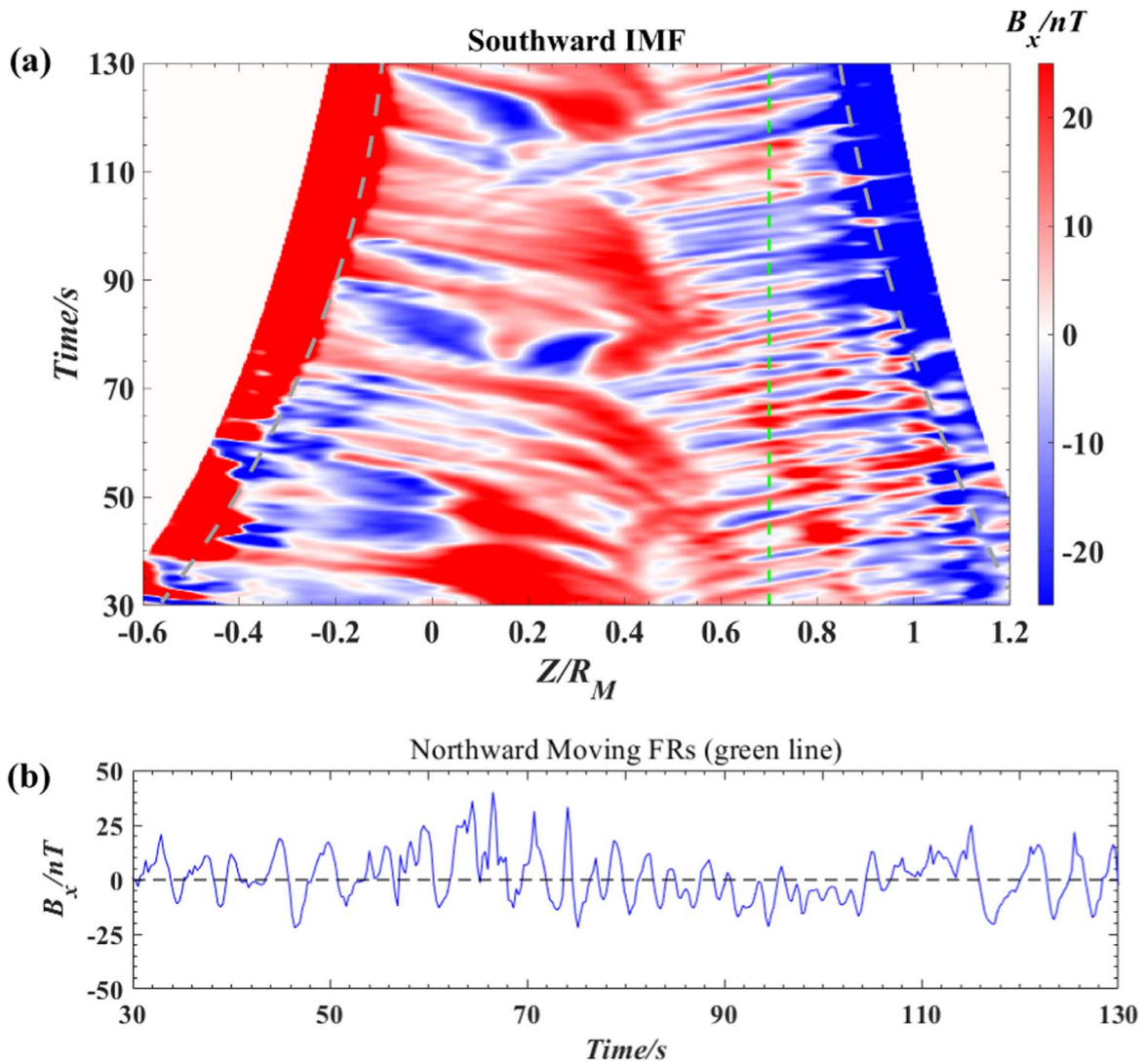


Figure 3. Stack plot of B_x along the magnetopause (denoted by the dashed line in Figure 2(b)) in the northern hemisphere at different times. The boundaries between the magnetopause and cusp are denoted by the gray dashed lines. (b) The evolution of B_x at $z = 0.7 R_M$ (green dashed line in (a)). The results are obtained in Case 1.

FTEs formed during magnetopause reconnection. The subsolar distance of the bow shock is about $1.5 R_M$, and the dayside magnetopause is close to Mercury’s surface. There are two flux ropes formed at the low-latitude dayside magnetopause, and there are six to seven flux ropes in the magnetotail. In this paper, we focus on the FTEs produced during dayside magnetopause reconnection. The magnetic structures of two FTEs (marked by “F1” and “F2,” respectively) can be clearly identified in Figure 2(b), which presents the enlarged view of the denoted region in Figure 2(a). In Figure 2(c), we show three components of the magnetic field (B_x , B_y , and B_z) and the ion number density N_i . Each FTE is characterized by a bipolar B_z and an increase in N_i . The size of these FTEs ranges from 0.05 to $0.50 R_M$ (i.e., 3 – $34 d_{i0}$).

Figure 3(a) exhibits the stack plot of B_x along the low-latitude dayside magnetopause, and (b) the evolution of B_x at $z = 0.7 R_M$ in Case 1. The FTEs are generated at about $z = 0.4 R_M$, and then propagate both northward and southward with a speed of about 90 km s^{-1} . The northward dipole offset from Mercury’s center leads to the generation of FTEs biased at about $z = 0.4 R_M$. An FTE shower can also be observed. There are about 25 FTEs produced in 100 s. A typical FTE has a

duration of about 2–3 s, and the separation between two neighboring FTE centers is about 4 s.

In Case 2, the IMF in the solar wind is purely northward, and its reconnection with Mercury’s magnetic field begins to occur in both the northern and southern hemispheres of the high-latitude nightside magnetopause at about $t = 45$ s. The characteristics of magnetic reconnection are similar in two hemispheres, and this is multiple X-line reconnection, where several X lines are simultaneously formed. Figure 4(a) plots the 3D view of Mercury’s magnetosphere obtained from our hybrid simulation at $t = 127.89$ s in Case 2, showing the ion number density N_i in the noon–midnight meridian and equatorial planes, magnetic field lines in the noon–midnight meridian plane, and the magnetic structures of FTEs formed during magnetopause reconnection. The subsolar distance of the magnetosphere is about $1.5 R_M$, which is consistent with the satellite observations (Slavin et al. 2008). A shock stands in front of the magnetopause, and its subsolar distance is about $1.9 R_M$. The ion number density is enhanced in the magnetosheath. There are six FTEs in total at this time, with three FTEs in the northern hemisphere and the other three FTEs in the southern hemispheres of the high-latitude nightside

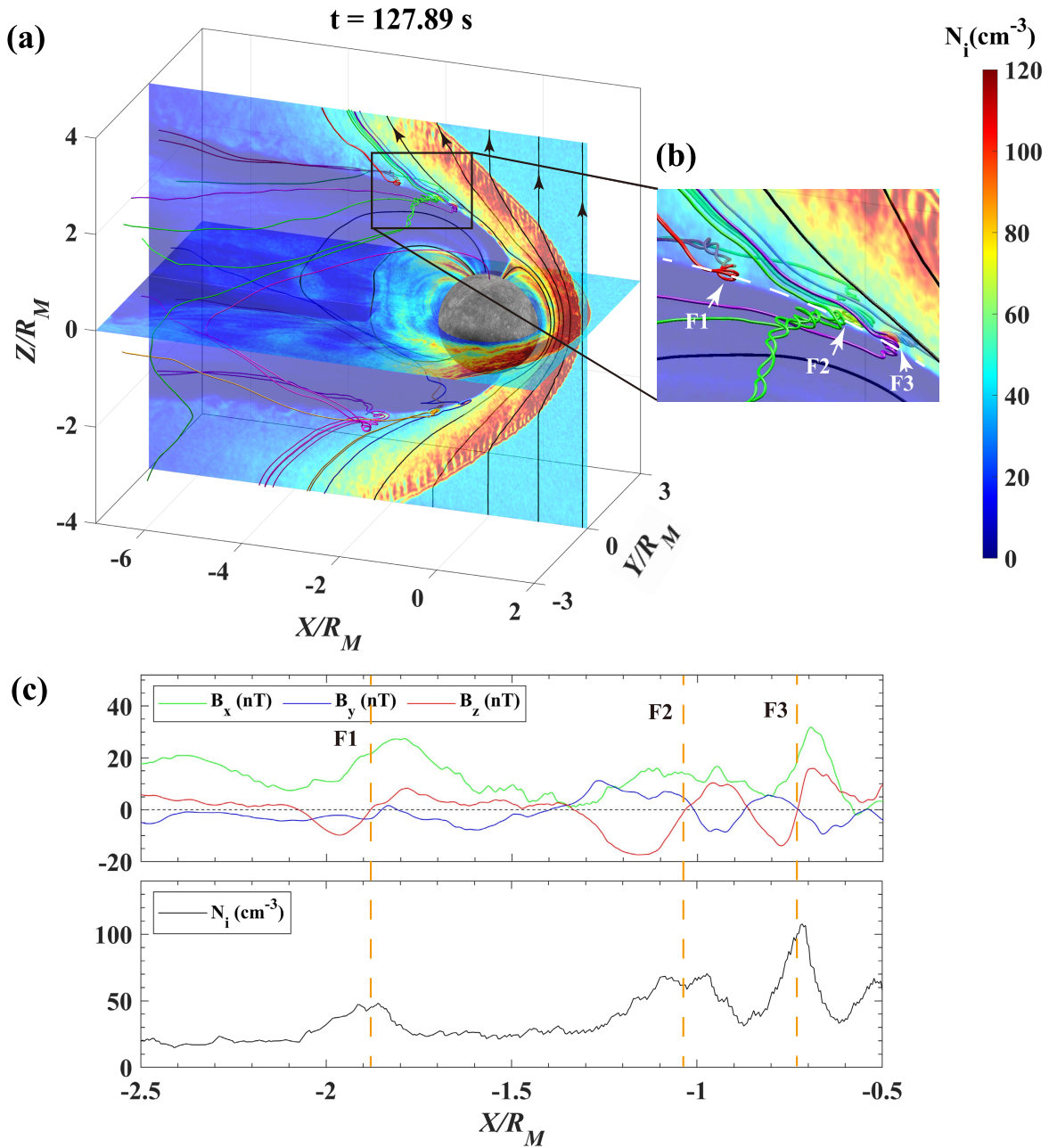


Figure 4. 3D view of Mercury’s magnetosphere obtained from our hybrid simulation at $t = 127.89$ s in Case 2. (a) The ion number density N_i in the noon–midnight meridian and equatorial planes. The magnetic structure of six FTEs is represented by 3D magnetic field lines with different colors (red, green, and violet). (b) The enlarged view of the denoted region in (a), and F1–3 represent three FTEs. (c) Three components of the magnetic field (B_x , B_y , and B_z) and the ion number density N_i along the dashed line in (b).

magnetopause. In these FTEs, one end of magnetic field line is connected to Mercury’s magnetic field, and the other to the IMF in the solar wind (not shown). The magnetic structures of three FTEs (marked by “F1,” “F2,” and “F3,” respectively) can be clearly identified in Figure 4(b), which presents the enlarged view of the denoted region in Figure 4(a). In Figure 4(c), we show three components of the magnetic field (B_x , B_y , and B_z) and the ion number density N_i . In each FTE, the component of magnetic field B_z has a bipolar structure, and the ion number density is enhanced, which are typical characteristics of FTE (Hasegawa et al. 2006).

Figure 5 exhibits the magnetic field lines and ion number density N_i in the northern hemisphere of the high-latitude

nightside magnetosphere at $t = 127.89$, 135.72, 143.55, and 160.78 s. As shown in Figure 4, at $t = 127.89$ s, there are three FTEs (F1, F2, and F3), and they move toward the magnetotail along the magnetopause until leaving away from the denoted region. These FTEs may coalesce with each other because of their different propagating speeds, and new FTEs are generated at the magnetopause near Mercury. The coalescence of FTEs is a re-reconnection process, which has also been well simulated and studied by performing 3D global hybrid simulations at the Earth’s magnetopause (Guo et al. 2021a, 2021b, 2021c) and ubiquitously observed in planetary magnetospheres (Wang et al. 2017; Zhou et al. 2017; Zhong et al. 2020). At $t = 135.72$ s, F2 and F3 have

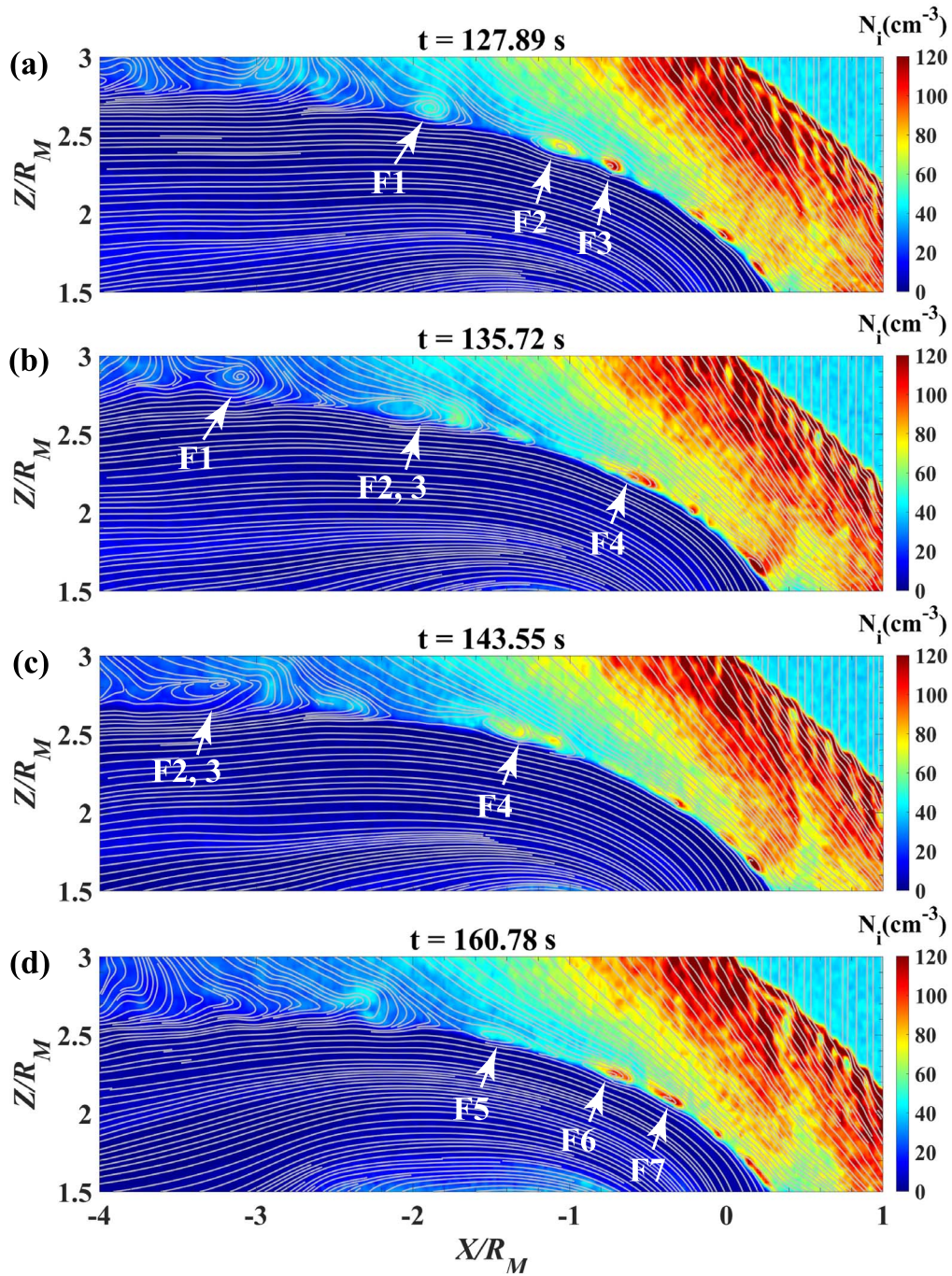


Figure 5. The magnetic field lines and ion number density N_i in the northern hemisphere of the high-latitude nightside magnetosphere (in the noon–midnight meridian plane) at $t =$ (a) 127.89, (b) 135.72, (c) 143.55, and (d) 160.78 s. The results are obtained in Case 2 and represented in the noon–midnight meridian plane, and F1–7 denote the positions of seven FTEs.

merged into one FTE “F2,3,” and a new FTE “F4” appears at about $x = -0.5R_M$. It needs to be noted that new FTEs can be generated at about $x = -0.5R_M$ continuously. At $t = 160.78$ s, there exist three new FTEs (F5, F6, and F7). A similar process is repeated in the late time. The size of these FTEs ranges from 0.15 to $0.56R_M$ (i.e., 10–40 d_{i0}).

Because the most salient feature of FTEs in the high-latitude nightside magnetopause is the bipolar structure in B_z , in Figure 6(a) we show a stack plot of B_z along the magnetopause in the northern hemisphere at different times to demonstrate the evolution of FTEs. At each time, there are about three to four

FTEs, and their propagation speed is about 250 km s^{-1} . During the whole time interval, we observe four events of FTE coalescence by following the dotted lines. These lines trace the trajectories of eight FTEs, which at last merge into four FTEs. Figure 6(b) presents the evolution of B_z at $x = -1.58R_M$, which is highly similar to the spacecraft observations. In a short time interval of 120 s or 2 minutes, there are about 20 FTEs. A typical FTE has a duration of about 2 s, and the separation between two neighboring FTE centers is about 6 s. Our simulations are consistent with FTE showers observed with the MESSENGER satellite (Slavin et al. 2012; Sun et al. 2020).

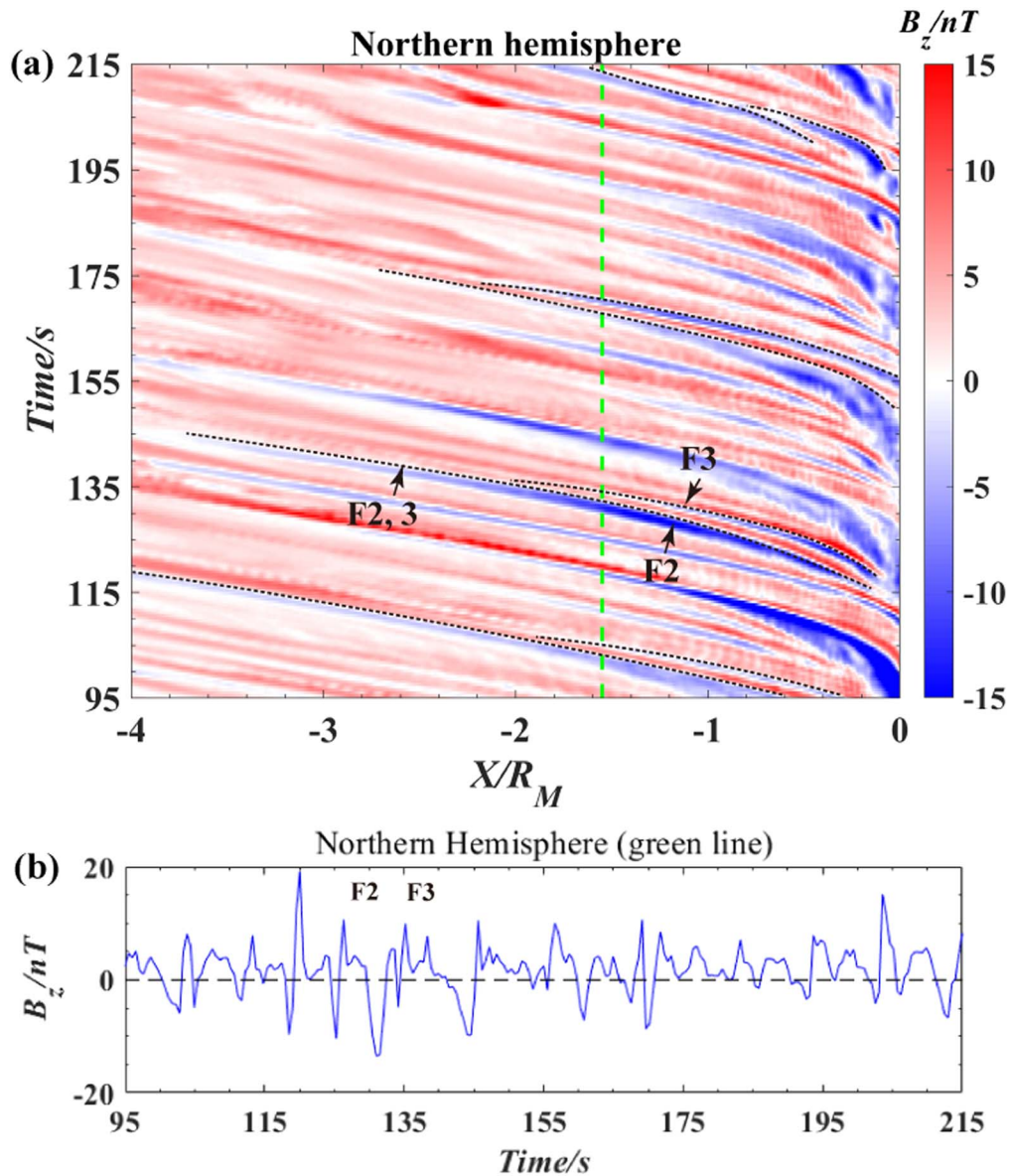


Figure 6. (a) The stack plot of B_z along the magnetopause (denoted by the dashed line in Figure 1(b)) in the northern hemisphere at different times, and the coalescence of FTEs is denoted by the black dotted lines. (b) The evolution of B_z at $x = -1.55R_M$ (green dashed line in (a)). The results are obtained in Case 2.

4. Conclusions and Discussion

Several global simulation models (including the magneto-hydrodynamic model, hybrid model, multifluid model, PIC model, etc.) have been successfully utilized to study the interactions between the solar wind and Mercury’s magnetosphere (e.g., Omidi et al. 2006; Travnicek et al. 2010; Müller et al. 2012; Richer et al. 2012; Chen et al. 2019; Dong et al. 2019; Jia et al. 2019; Fatemi et al. 2020; Lapenta et al. 2022), and with a two-dimensional (2D) hybrid simulation model Omidi et al. (2006) found that FTEs can be produced in the dayside magnetopause when the IMF is southward. In this paper, by performing a global hybrid simulation code named as gcPIC-hybrid, we identified FTE showers at Mercury’s magnetopause, which is the first time that FTE showers have been reproduced in Mercury’s global simulation model. Two cases with the purely southward and northward IMF in the solar wind have been run. Consistent with the observations from MESSENGER (Slavin et al. 2012; Sun et al. 2020), FTE

showers, i.e., tens of FTEs produced in 1–2 minutes, have been identified at the magnetopause. When the IMF is purely southward, FTE showers are generated at the low-latitude dayside magnetopause, and the FTEs with a size ranging from 0.05 to 0.50 R_M can propagate toward the southward or northward with a propagation speed of about 90 km s^{-1} . When the IMF is purely northward, FTE showers appear in both the southern and northern hemispheres of the high-latitude nightside magnetopause, and the FTEs with a size ranging from 0.15 to 0.56 R_M propagate toward the magnetotail with a speed of about 250 km s^{-1} .

FTE showers are a series of FTEs observed by spacecraft in a short time interval. Based on our simulations, we can find that FTEs are continuously generated in limited regions of Mercury’s magnetopause, and then leave away with a high speed. Therefore, a satellite at the magnetopause will observe plenty of FTEs in a short time interval, which is the FTE showers observed by MESSENGER (Slavin et al. 2012; Sun et al. 2020). When the IMF is southward, a typical FTE formed

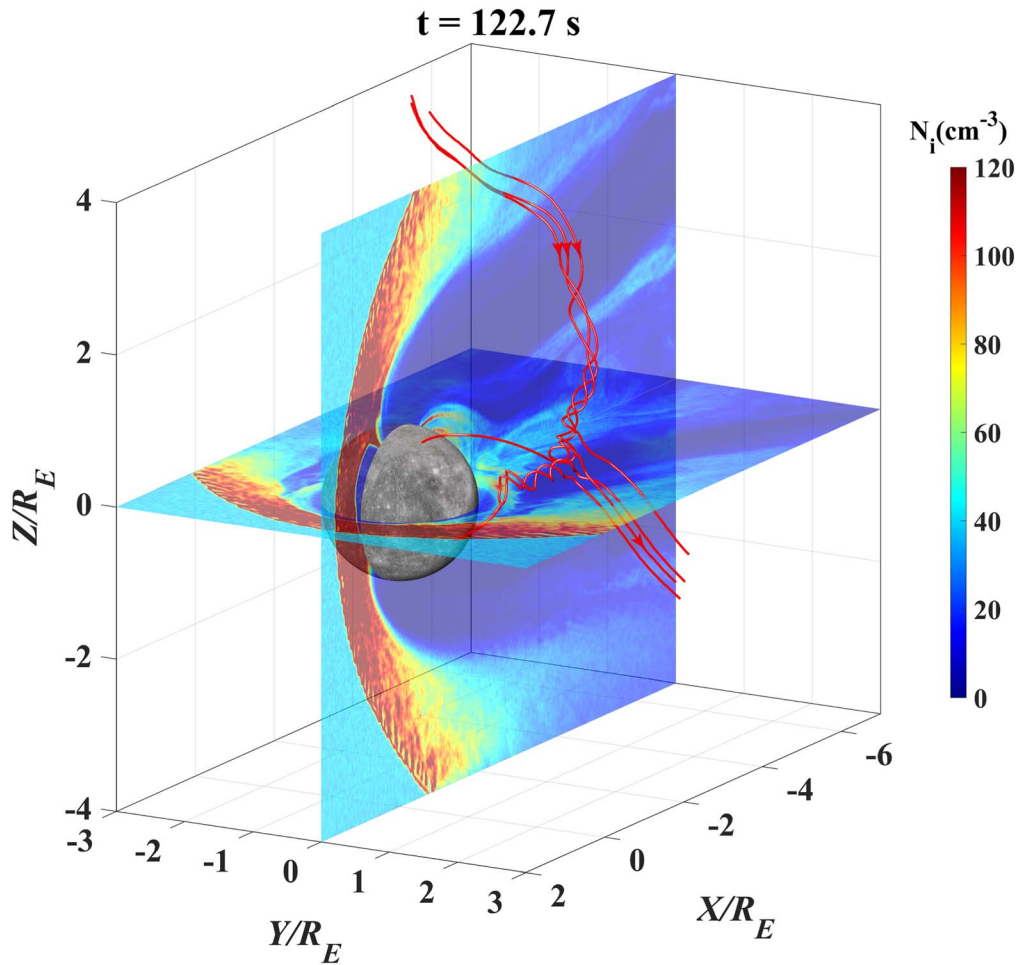


Figure 7. The structure of FTE obtained from the simulation at $t = 122.7$ s. The red lines are the magnetic field lines associated with the FTE. The ion number density N_i in the noon–midnight meridian and equatorial planes is also plotted. The simulation parameters are the same as those in Cases 1 and 2, except that the IMF is $\mathbf{B}_0 = (0, 14.1, -14.1)$ nT.

at the dayside magnetopause has a duration of about 2 s. The duration of a typical FTE at the nightside magnetopause is about 2–3 s when the IMF has a northward component, which is consistent with the observation of an FTE shower reported by Slavin et al. (2012). However, when modeling the shape of FTEs, they assumed the propagation speed to be 400 km s^{-1} , and the mean semimajor axis was about 374 km or $0.15 R_M$. According to our simulations, the propagation speed of FTE formed at the nightside magnetopause is about 250 km s^{-1} . Therefore, the size of the FTEs may be overestimated in Slavin et al. (2012).

In Case 1, the IMF is purely southward, and the FTEs generated at the low-latitude dayside magnetopause have a bipolar structure of B_x . In Case 2, when the IMF is purely northward, a bipolar structure of B_z appears in the FTEs in both the southern and northern hemispheres of the high-latitude nightside magnetopause. However, the FTEs observed in Slavin et al. (2009) when the IMF has a southward component have been reported to have a bipolar structure of B_y . We attribute such kinds of FTEs to the effect of the y component of the IMF. We examine a case with the IMF $\mathbf{B}_0 = (0, 14.1, -14.1)$ nT, and the other parameters are the same as those in Cases 1 and 2. The FTEs are first formed at the dayside magnetopause, and they have a bipolar structure of B_x . Then, they move toward the nightside along the magnetopause flanks, and their structure

becomes distorted. When these FTEs reach the nightside, a bipolar structure of B_y can be formed. Figure 7 plots the structure of such a kind of FTE obtained from the simulation at $t = 122.7$ s. The axis of the FTE almost aligns along the z direction in the nightside. When the FTE moves toward the nightside, a bipolar structure of B_y can be observed.

We wish to acknowledge the useful discussion with C. F. Dong on this work. This research was funded by the Strategic Priority Research Program of Chinese Academy of Sciences grant No. XDB41000000, the National Science Foundation of China (NSFC) grant 42174181, Key Research Program of Frontier Sciences CAS (QYZDJ-SSW-DQC010). Computer resources were provided by the Hefei Advanced Computing Center of China. The authors gratefully acknowledge the data resources from the “National Space Science Data Center, National Science & Technology Infrastructure of China. (<http://www.nssdc.ac.cn>).” In this study, the simulation data that are used to plot the figures all can be downloaded from doi:10.12176/01.99.02919.

ORCID iDs

Quanming Lu <https://orcid.org/0000-0003-3041-2682>
 Jin Guo <https://orcid.org/0000-0002-9950-1029>
 San Lu <https://orcid.org/0000-0003-2248-5072>

James A. Slavin  <https://orcid.org/0000-0002-9206-724X>
 Weijie Sun  <https://orcid.org/0000-0001-5260-658X>
 Rongsheng Wang  <https://orcid.org/0000-0002-9511-7660>
 Jun Zhong  <https://orcid.org/0000-0003-4187-3361>

References

- Anderson, B. J., Acuña, M. H., Korth, H., et al. 2008, *Sci*, **321**, 82
 Anderson, B. J., Johnson, C. L., Korth, H., et al. 2011, *Sci*, **333**, 1859
 Chen, Y., Tóth, G., Jia, X., et al. 2019, *JGRA*, **124**, 8954
 Dong, C., Wang, L., Hakim, A., et al. 2019, *GeoRL*, **46**, 11584
 Dong, X. C., Dunlop, M. W., Trattner, K. J., et al. 2017, *GeoRL*, **44**, 5951
 Fatemi, S., Poppe, A. R., & Barabash, S. 2020, *JGR*, **125**, e2019JA027706
 Fuselier, S. A., Petrinec, S. M., Trattner, K. J., et al. 2018, *JGRA*, **123**, 8407
 Guo, J., Lu, S., Lu, Q., et al. 2021a, *GeoRL*, **48**, e2021GL095003
 Guo, J., Lu, S., Lu, Q., et al. 2021b, *JGR*, **126**, e2020JA028670
 Guo, J., Lu, S., Lu, Q., et al. 2021c, *JGR*, **126**, e2021JA029388
 Guo, Z., Lin, Y., Wang, X., et al. 2020, *JGR*, **125**, e2020JA027795
 Hasegawa, H., Sonnerup, B. U. Ö., Owen, C. J., et al. 2006, *AnGeo*, **24**, 603
 Jasinski, J. M., Slavin, J. A., Arridge, C. S., et al. 2016, *GeoRL*, **43**, 6713
 Jia, X., Slavin, J. A., Poh, G., et al. 2019, *JGR*, **124**, 229
 Kuznetsova, M. M., Sibeck, D. G., Hesse, M., et al. 2009, *GeoRL*, **36**, L10104
 Lapenta, G., Schriver, D., Walker, R. J., et al. 2022, *JGR*, **127**, e2021JA030241
 Lee, L. C., & Fu, Z. F. 1985, *GeoRL*, **12**, 105
 Lockwood, M., & Moen, J. 1999, *AnGeo*, **17**, 996
 Lu, Q., Ke, Y., Wang, X., et al. 2019, *JGR*, **124**, 4157
 Müller, J., Simon, S., Wang, Y.-C., et al. 2012, *Icar*, **218**, 666
 Omidi, N., Blanco-Cano, X., Russell, C. T., & Karimabadi, H. 2006, *AdSpR*, **38**, 632
 Paschmann, G., Haerendel, G., Papamastorakis, I., et al. 1982, *JGR*, **87**, 2159
 Richer, E., Modolo, R., Chanteur, G. M., Hess, S., & Leblanc, F. 2012, *JGR*, **117**, A10228
 Rijnbeek, R. P., Cowley, S. W. H., Southwood, D. J., & Russell, C. T. 1984, *JGR*, **89**, 786
 Russell, C. T., & Elphic, R. C. 1978, *SSRv*, **22**, 681
 Russell, C. T., & Walker, R. J. 1985, *JGR*, **90**, 11067
 Slavin, J. A., Acuña, M. H., Anderson, B. J., et al. 2008, *Sci*, **321**, 85
 Slavin, J. A., DiBraccio, G. A., Gershman, D. J., et al. 2009, *Sci*, **324**, 606
 Slavin, J. A., Imber, S. M., Boardsen, S. A., et al. 2012, *JGR*, **117**, A00M06
 Sun, W., Slavin, J. A., Milillo, A., et al. 2022, *JGR*, **127**, e2022JA030280
 Sun, W. J., Slavin, J. A., Smith, A. W., et al. 2020, *GeoRL*, **47**, e2020GL089784
 Tan, B., Lin, Y., Perez, J. D., & Wang, X. Y. 2011, *JGR*, **116**, A02206
 Travnicek, P. M., Schriver, D., Hellinger, P., et al. 2010, *Icar*, **209**, 11
 Wang, R. S., Lu, Q. M., Nakamura, R., et al. 2017, *JGR*, **122**, 10436
 Zhong, J., Pu, Z. Y., Dunlop, M. W., et al. 2013, *JGR*, **118**, 1904
 Zhong, J., Wei, Y., & Lee, L. C. 2020, *ApJL*, **893**, L18
 Zhou, M., Berchem, J., Walker, R. J., et al. 2017, *PhRvL*, **119**, 055101